A high-order scheme for the numerical simulation of high-enthalpy hypersonic flows

D. Passiatore*, L. Sciacovelli**, P. Cinnella*** and G. Pascazio*
Corresponding author: donatella.passiatore@poliba.it

* Politecnico di Bari, DMMM, via Re David 200, 70125 Bari, Italy.
** Arts et Métiers, DynFluid Laboratory, 151 bd. de l'Hôpital, 75013 Paris, France.
*** Sorbonne Université, Institut Jean Le Rond d'Alembert, 4 Place Jussieu, 75005 Paris, France.

Abstract: A high-order shock-capturing finite-difference scheme for scale-resolving numerical simulations of hypersonic high-enthalpy flows, involving thermal non-equilibrium effects, is presented. The suitability of the numerical strategy for such challenging configurations is assessed in terms of accuracy and robustness, with special focus on shock-capturing capabilities. The approach is demonstrated for a variety of thermochemical non-equilibrium configurations.

Keywords: compressible flows, shocks, thermochemical non-equilibrium, high-order methods

1   Introduction

High-enthalpy flows are encountered in many fields related to the aerospace industry. These flows are characterized by the presence of thermodynamic processes having a major influence on the performance of vehicles flying at hypersonic speeds, such as gas dissociation, vibrational relaxation, surface ablation or ionization [1]. The rate at which these different processes evolve are highly dependent on the local thermodynamic conditions and can be of the same order of the natural timescales of the flow, resulting in a nonequilibrium state. The overall picture is even further complicated when turbulence comes into play, because of the wide range of spatial and temporal scales involved. Carrying out numerical simulations of high-enthalpy turbulent flows is an extremely challenging task requiring the use of suitable numerical methods, which must be properly designed in order to meet the concurrent needs of ensuring a sufficient numerical robustness and an accurate representation of the flow scales to be resolved. Recently, Sciacovelli *et al.* [2] presented a high-order centred finite-difference scheme for the computation of compressible flows with shock waves, using tenth-order accurate approximations for the non linear fluxes supplemented with a higher-order extension of Jameson's adaptive artificial dissipation [3]. The overall order of accuracy of the artificial viscosity term ensures a dissipative-dominant error, reducing the appearance and amplification of spurious oscillations. The numerical scheme has been successfully applied to the simulation of turbulent high-speed flows of dense gases [4] and to flows with finite-rate chemistry effects [2]. In this study, we present an extension of such technique to flows with vibrational relaxation processes. This strategy, recently employed by Passiatore *et al.* [5] to perform a Direct Numerical Simulation (DNS) of a boundary layer undergoing laminar-to-turbulent transition in thermochemical nonequilibrium conditions, is here tested in high-gradient flow configurations to verify its capabilities in handling strong flow discontinuities. The paper is organised as follows. The governing equations and the thermochemical models are described in Section 2. The numerical method and its extension for thermal nonequilibrium flows are shown in Section 3, whereas Section 4 presents a selected list of test cases of increasing complexity. Conclusions are then drawn in Section 5.

2 Governing Equations

In this work, the fluid under investigation is air at high-temperature, thermally and chemically out-of-equilibrium, modeled as a neutral five-species mixture of N_2, O_2, NO, O. Therefore, the governing equations are the compressible Navier–Stokes equations for multicomponent chemically-reacting and thermally-relaxing gases [6], which read:

$$\frac{\partial \rho}{\partial t} + \frac{\partial \rho u_j}{\partial x_j} = 0 \tag{1}$$

$$\frac{\partial \rho u_i}{\partial t} + \frac{\partial (\rho u_i u_j + p \delta_{ij})}{\partial x_j} = \frac{\partial \tau_{ij}}{\partial x_j} \tag{2}$$

$$\frac{\partial \rho E}{\partial t} + \frac{\partial \left[(\rho E + p) u_j \right]}{\partial x_j} = \frac{\partial (u_i \tau_{ij})}{\partial x_j} - \frac{\partial (q_j^{\mathrm{TR}} + q_j^{\mathrm{V}})}{\partial x_j} - \frac{\partial}{\partial x_j} \left(\sum_{n=1}^{\mathrm{NS}} \rho_n u_{nj}^D h_n \right) \tag{3}$$

$$\frac{\partial \rho_n}{\partial t} + \frac{\partial (\rho_n u_j)}{\partial x_j} = -\frac{\partial \rho_n u_{nj}^D}{\partial x_j} + \dot{\omega}_n \qquad (n = 1, .., \mathrm{NS} - 1) \tag{4}$$

$$\frac{\partial \rho e_{\mathrm{V}}}{\partial t} + \frac{\partial \rho e_{\mathrm{V}} u_j}{\partial x_j} = \frac{\partial}{\partial x_j} \left(-q_j^{\mathrm{V}} - \sum_{m=1}^{\mathrm{NM}} \rho_m u_{mj}^D e_{\mathrm{V}m} \right) + \sum_{m=1}^{\mathrm{NM}} \left(Q_{\mathrm{TV}m} + \dot{\omega}_m e_{\mathrm{V}m} \right). \tag{5}$$

In the preceding formulation, ρ is the mixture density, t the time coordinate, x_j the space coordinate in the j-th direction of a Cartesian coordinate system, with u_j the velocity vector component in the same directions, p is the pressure and τ_{ij} the viscous stress tensor, modeled as

$$\tau_{ij} = \mu \left(\frac{\partial u_i}{\partial x_j} + \frac{\partial u_j}{\partial x_i} \right) - \frac{2}{3} \mu \frac{\partial u_k}{\partial x_k} \delta_{ij}, \tag{6}$$

with μ the mixture dynamic viscosity and δ_{ij} the Kronecker symbol. The conservation of total energy $E = e + \frac{1}{2} u_i u_i$ is expressed by means of equation (3), where e is the mixture internal energy, $q_j^{\mathrm{TR}} = -\lambda_{\mathrm{TR}} \frac{\partial T}{\partial x_j}$ and $q_j^{\mathrm{V}} = -\lambda_{\mathrm{V}} \frac{\partial T_V}{\partial x_j}$ are the roto-translational and vibrational contribution to the heat flux, λ_{TR} and λ_{V} being the roto-translational and vibrational thermal conductivities, respectively. In such formulation, we are considering two temperatures, T being the roto-translational one and T_V the vibrational temperature. u_{nj}^D denotes the diffusion velocity and h_n the specific enthalpy for the n-th species. In the species conservation equations (4), $\rho_n = \rho Y_n$ represents the n-th species partial density (Y_n being the mass fraction) and $\dot{\omega}_n$ the rate of production of the n-th species. To ensure total mass conservation, the mixture density and NS-1 species conservation equations are solved, while the density of the NS-th species is computed as $\rho_{\mathrm{NS}} = \rho - \sum_{n=1}^{\mathrm{NS}-1} \rho_n$. In the following, we set such species as molecular nitrogen, since it is the most abundant one throughout the computational domain. As for equation (5), $e_{\mathrm{V}} = \sum_{m=1}^{\mathrm{NM}} Y_m e_{\mathrm{V}m}$ represents the mixture vibrational energy, with $e_{\mathrm{V}m}$ the vibrational energy of the m-th molecule and NM their total number. Only one additional equation for the conservation of mixture vibrational energy is employed, relying on the assumption that the vibrational energetic modes of the three molecular species in the mixture are equilibrated with each other at the same T_V. In the same equation, $Q_{\mathrm{TV}} = \sum_{m=1}^{\mathrm{NM}} Q_{\mathrm{TV}m}$ represents the energy exchange between vibrational and translational modes due to molecular collisions and $\sum_{m=1}^{\mathrm{NM}} \dot{\omega}_m e_{\mathrm{V}m}$ the vibrational energy lost or gained due to molecular depletion or production. Each species is assumed to behave as a thermally-perfect gas; Dalton's pressure mixing law leads then to the thermal equation of state:

$$p = \rho T \sum_{n=1}^{\mathrm{NS}} \frac{\mathcal{R} Y_n}{\mathcal{M}_n} = T \sum_{n=1}^{\mathrm{NS}} \rho_n R_n, \tag{7}$$

R_n and $\mathcal{M}_n$ being the gas constant and molecular weight of the n-th species, respectively, and $\mathcal{R} = 8.314$ J/mol K the universal gas constant. The thermodynamic properties of high-temperature air species are

computed considering the contributions of translational, rotational and vibrational (TRV) modes:

$$e = \sum_{n=1}^{\mathrm{NS}} Y_n h_n - \frac{p}{\rho} = h - \frac{p}{\rho}, \quad \text{with} \quad h_n = h_{f,n}^0 + h_n^{\mathrm{TR}} + e_{Vn}. \tag{8}$$

Here, $h_{f,n}^0$ is the n-th species enthalpy of formation at the reference temperature ($T_{\mathrm{ref}} = 298.15\,\mathrm{K}$), h_n^{TR} is the roto-translational specific enthalpy and e_{Vn} the vibrational energy of species n. These terms read:

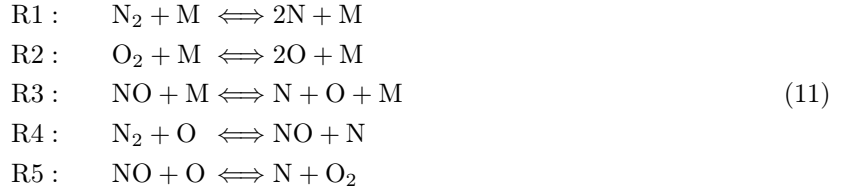$$h_n^{\mathrm{TR}} = \int_{T_{\mathrm{ref}}}^{T} (c_{p,n}^{\mathrm{T}} + c_{p,n}^{\mathrm{R}})\, \mathrm{d}T' \quad \text{with} \quad c_{p,n}^{\mathrm{T}} = \frac{5}{2} R_n, \quad c_{p,n}^{\mathrm{R}} = \begin{cases} R_n & \text{for diatomic species} \\ 0 & \text{for monoatomic species} \end{cases} \tag{9}$$

and

$$e_{Vn} = \begin{cases} \frac{\theta_n R_n}{\exp(\theta_n/T_{\mathrm{V}}) - 1} & \text{for diatomic species} \\ 0 & \text{for monoatomic species} \end{cases} \tag{10}$$

with θ_n the characteristic vibrational temperature of each molecule ($3393\,\mathrm{K}$, $2273\,\mathrm{K}$ and $2739\,\mathrm{K}$ for N_2, O_2 and NO, respectively). After the numerical integration of the conservation equations, the roto-translational temperature T is computed from the specific internal energy (devoid of the vibrational contribution) directly, whereas an iterative Newton–Raphson method is used to compute T_{V} from $e_{\mathrm{V}} = \sum_{m=1}^{\mathrm{NM}} Y_m e_{Vm}$.

To close the system, we use Park's two-temperatures (2T) model [7] to take into account the contextual presence of thermal and chemical non-equilibrium for the computation of $\dot{\omega}_n$ and Q_{TV}. Specifically, the five species interact with each other through a reaction mechanism consisting of five reversible chemical steps [8]:

$$\begin{aligned}
\text{R1}: && N_2 + M &\Longleftrightarrow 2N + M \\
\text{R2}: && O_2 + M &\Longleftrightarrow 2O + M \\
\text{R3}: && NO + M &\Longleftrightarrow N + O + M \\
\text{R4}: && N_2 + O &\Longleftrightarrow NO + N \\
\text{R5}: && NO + O &\Longleftrightarrow N + O_2
\end{aligned} \tag{11}$$

M being the third body (any of the five species considered). Dissociation and recombination processes are described by reactions R1, R2 and R3, whereas the shuffle reactions R4 and R5 represent rearrangement processes. The mass rate of production of the n-th species is governed by the law of mass action:

$$\dot{\omega}_n = \mathcal{M}_n \sum_{r=1}^{\mathrm{NR}} (\nu_{nr}'' - \nu_{nr}') \times \left[k_{f,r} \prod_{n=1}^{\mathrm{NS}} \left(\frac{\rho Y_n}{\mathcal{M}_n} \right)^{\nu_{nr}'} - k_{b,r} \prod_{n=1}^{\mathrm{NS}} \left(\frac{\rho Y_n}{\mathcal{M}_n} \right)^{\nu_{nr}''} \right], \tag{12}$$

where ν_{nr}' and ν_{nr}'' are the stoichiometric coefficients for reactants and products in the r-th reaction for the n-th species, respectively, and NR is the total number of reactions. Furthermore, $k_{f,r}$ and $k_{b,r}$ denote the forward and backward rates of reaction r, modeled by means of Arrhenius' law. The coupling between chemical and thermal nonequilibrium is taken into account by means of a modification of the temperature values used for computing the reaction rates. Indeed, a geometric-averaged temperature is considered for the dissociation reactions R1, R2 and R3 in (11), computed as $T_{\mathrm{avg}} = T^q T_{\mathrm{V}}^{1-q}$ with $q = 0.7$ [7].

Lastly, the vibrational-translational energy exchange is computed as:

$$Q_{\mathrm{TV}} = \sum_{m=1}^{\mathrm{NM}} Q_{\mathrm{TV},m} = \sum_{m=1}^{\mathrm{NM}} \rho_m \frac{e_{\mathrm{V}m}(T) - e_{\mathrm{V}m}(T_{\mathrm{V}})}{\tau_m}, \tag{13}$$

where τ_m is the corresponding relaxation time evaluated by means of the expression [9]:

$$\tau_m = \sum_{n=1}^{\mathrm{NS}} \frac{\rho_n}{\mathcal{M}_n} \sum_{n=1}^{\mathrm{NS}} \frac{\tau_{mn}}{\rho_n/\mathcal{M}_n}. \tag{14}$$

Here, τ_{mn} is the relaxation time of the m-th molecule with respect to the n-th species, computed as the sum of two contributions

$$\tau_{mn} = \tau_{mn}^{MW} + \tau_{mn}^{c}. \tag{15}$$

The first term writes:

$$\tau_{mn}^{\text{MW}} = \frac{p}{p_{\text{atm}}} \exp\left[a_{mn}(T^{-\frac{1}{3}} - b_{mn}) - 18.42\right], \tag{16}$$

where $p_{\text{atm}} = 101325\,\text{Pa}$ and a_{mn} and b_{mn} are coefficients reported in [10]. Since this expression tends to underestimate the experimental data at temperatures above $5000\,\text{K}$, a high-temperature correction was proposed by Park [11]:

$$\tau_{mn}^{c} = \sqrt{\frac{\phi_{mn}}{\mathcal{M}_m \sigma}}, \tag{17}$$

where $\phi_{mn} = \frac{\mathcal{M}_m \mathcal{M}_n}{\mathcal{M}_m + \mathcal{M}_n}$ and $\sigma = \sqrt{\frac{8\mathcal{R}}{T\pi}} \frac{7.5\times 10^{-12}\text{NA}}{T}$, NA being Avogadro's number.

As for the computation of the transport properties, pure species' viscosity and thermal conductivities are computed using curve-fits by Blottner [12] and Eucken's relations [13], respectively. The corresponding mixture properties are evaluated by means of Wilke's mixing rules [14]. Mass diffusion is modeled by means of Fick's law:

$$\rho_n u_{nj}^D = -\rho D_n \left(\frac{\partial Y_n}{\partial x_j} + Y_n \frac{\partial \ln\mathcal{M}}{\partial x_j}\right) + \rho_n \sum_{n=1}^{\text{NS}} D_n \left(\frac{\partial Y_n}{\partial x_j} + Y_n \frac{\partial \ln\mathcal{M}}{\partial x_j}\right), \tag{18}$$

where the first term on the r.h.s. represents the effective diffusion velocity and the second one is a mass corrector term that should be taken into account in order to satisfy the continuity equation when dealing with non-constant species diffusion coefficients [15]. Specifically, D_n is an equivalent diffusion coefficient of species n into the mixture, computed following Hirschfelder's approximation [13], starting from the binary diffusion coefficients which are curve-fitted in [16]. Further details about the selected models and the underling hypotheses can be found in Passiatore *et al.* [5].

3 Numerical method

The governing equations presented in the previous section are integrated numerically by using the numerical scheme presented in Sciacovelli *et al.* [2]. In the following, we briefly recall the numerical strategy and we detail its extension to thermally out-of-equilibrium flows. Let us consider a 1D system of hyperbolic conservation laws:

$$\frac{\partial w}{\partial t} + \frac{\partial f(w)}{\partial x} = 0 \tag{19}$$

where w denotes the vector of conservative variables and $f(w)$ the flux function. A conservative semi-discrete approximation of the spatial derivatives writes

$$\left(\frac{\partial w}{\partial t}\right)_j + \frac{(\delta\mathcal{F})_j}{\delta x} = 0 \tag{20}$$

where $\mathcal{F}$ denotes the numerical flux and δ is the classical difference operator over one cell

$$(\delta\bullet)_j := (\bullet)_{j+\frac{1}{2}} - (\bullet)_{j-\frac{1}{2}}. \tag{21}$$

The flux derivatives are approximated by means of a purely centered tenth-order operator, supplemented with a nonlinear adaptive artificial term. The resulting numerical flux at cell interface $j+\frac{1}{2}$, $\mathcal{F}_{j+\frac{1}{2}}$ takes the following form:

$$\mathcal{F}_{j+\frac{1}{2}} = \mathcal{H}_{j+\frac{1}{2}} - \mathcal{D}_{j+\frac{1}{2}}. \tag{22}$$

4

with $\mathcal{H}_{j+\frac{1}{2}}$ the consistent (central) part and $\mathcal{D}_{j+\frac{1}{2}}$ the dissipative part. For a scheme of order $2P + 3$ with a stencil of $2(P + 2) + 1$ points, the centered term reads:

$$\mathcal{H}_{j+\frac{1}{2}} = \left[\left(I - \sum_{p=0}^{P} a_p \delta^{2+2p} \right) \mu f \right]_{j+\frac{1}{2}}, \tag{23}$$

where μ denotes the cell-average operator, namely:

$$(\mu \bullet)_{j+\frac{1}{2}} := \frac{1}{2} \left[(\bullet)_{j+1} + (\bullet)_j \right]. \tag{24}$$

The coefficients a_p have alternate negative and positive signs as P increases. For the sake of clarity, we give hereafter the expressions of the schemes of order 4 to 10 of the preceding family:

$$\mathcal{H}_{j+\frac{1}{2}} = \left[\left(I - \frac{1}{6}\delta^2 \right) \mu f \right]_{j+\frac{1}{2}} \qquad \text{(order 4)} \tag{25}$$

$$\mathcal{H}_{j+\frac{1}{2}} = \left[\left(I - \frac{1}{6}\delta^2 + \frac{1}{30}\delta^4 \right) \mu f \right]_{j+\frac{1}{2}} \qquad \text{(order 6)} \tag{26}$$

$$\mathcal{H}_{j+\frac{1}{2}} = \left[\left(I - \frac{1}{6}\delta^2 + \frac{1}{30}\delta^4 - \frac{1}{140}\delta^6 \right) \mu f \right]_{j+\frac{1}{2}} \qquad \text{(order 8)} \tag{27}$$

$$\mathcal{H}_{j+\frac{1}{2}} = \left[\left(I - \frac{1}{6}\delta^2 + \frac{1}{30}\delta^4 - \frac{1}{140}\delta^6 + \frac{1}{630}\delta^8 \right) \mu f \right]_{j+\frac{1}{2}} \qquad \text{(order 10)} \tag{28}$$

The dissipative term, with the double role of damping grid-to-grid oscillations in smooth regions and controlling the appearence of spurious oscillations in the vicinity of flow discontinuities, is a nonlinear blending of a high-order dissipation and a low order shock capturing term, of the form:

$$\mathcal{D}_{j+\frac{1}{2}} = \rho(A)_{j+\frac{1}{2}} \left[\varepsilon_2 \delta w + (-1)^{(P+1)} \varepsilon_{2(P+2)} \delta^{(2P+3)} w \right]_{j+\frac{1}{2}} \tag{29}$$

with

$$\varepsilon_{2 j+\frac{1}{2}} = k_2 \max(\varphi_j, \varphi_{j+1}), \qquad \varepsilon_{2(P+2) j+\frac{1}{2}} = \max(0, k_{2(P+2)} - k_\varepsilon \varepsilon_{2 j+\frac{1}{2}}), \tag{30}$$

where $\rho(A)$ is the spectral radius of the flux Jacobian matrix A, whereas k_2 and $k_{2(P+2)}$ are adjustable dissipation coefficients and k_ε is a constant equal to a_0/a_P, determining the threshold below which the higher-order dissipation is switched off. For schemes of order 3 to 9, this gives the following expressions:

$$\mathcal{D}_{j+\frac{1}{2}} = \rho(A)_{j+\frac{1}{2}} \left[\varepsilon_2 \delta w - \varepsilon_4 \delta^3 w \right]_{j+\frac{1}{2}} \qquad \varepsilon_{4 j+\frac{1}{2}} = \max(0, k_4 - \varepsilon_{2 j+\frac{1}{2}}) \qquad \text{(order 3)} \tag{31}$$

$$\mathcal{D}_{j+\frac{1}{2}} = \rho(A)_{j+\frac{1}{2}} \left[\varepsilon_2 \delta w + \varepsilon_6 \delta^5 w \right]_{j+\frac{1}{2}} \qquad \varepsilon_{6 j+\frac{1}{2}} = \max(0, k_6 - \frac{1}{5}\varepsilon_{2 j+\frac{1}{2}}) \qquad \text{(order 5)} \tag{32}$$

$$\mathcal{D}_{j+\frac{1}{2}} = \rho(A)_{j+\frac{1}{2}} \left[\varepsilon_2 \delta w - \varepsilon_8 \delta^7 w \right]_{j+\frac{1}{2}} \qquad \varepsilon_{8 j+\frac{1}{2}} = \max(0, k_8 - \frac{3}{70}\varepsilon_{2 j+\frac{1}{2}}) \qquad \text{(order 7)} \tag{33}$$

$$\mathcal{D}_{j+\frac{1}{2}} = \rho(A)_{j+\frac{1}{2}} \left[\varepsilon_2 \delta w + \varepsilon_{10} \delta^9 w \right]_{j+\frac{1}{2}} \qquad \varepsilon_{10 j+\frac{1}{2}} = \max(0, k_{10} - \frac{1}{105}\varepsilon_{2 j+\frac{1}{2}}) \qquad \text{(order 9)} \tag{34}$$

The activation of the lower-order dissipation component is governed by the shock sensor φ_j, whose general formulation writes

$$\varphi_j = \frac{(\nabla \cdot \mathbf{u})^2}{(\nabla \cdot \mathbf{u})^2 + |\nabla \times \mathbf{u}|^2 + \epsilon} \times \left| \frac{p_{j+1} - 2p_j + p_{j-1}}{p_{j+1} + 2p_j + p_{j-1}} \right| \tag{35}$$

The two terms in equation (35) denote the classical Ducros' [17] and Jameson's pressure-based [3] shock sensors, respectively, ϵ being a small positive value to avoid division by zero. Note that, differently from the strategy of Sciacovelli *et al.* [2], the Ducros' sensor modification of Bhagatwala & Lele [18] is not considered here, since its addition would require larger k_2 values in order to ensure a proper amount of numerical dissi-

pation close to flow discontinuities for the configurations under investigation. With the above definitions, the resulting numerical approximation of the inviscid terms is $(2P + 1)^{\text{th}}$-order accurate in smooth flow region and becomes 1st-order accurate close to flow discontinuities.

A modification to the shock sensor is introduced in order to deal with thermochemical non-equilibrium. For such flows the pressure-based shock sensor, is not suitable to detect regions with steep vibrational energy gradients since p and T_V are not directly linked through the equation of state. A specific control is then introduced for the vibrational energy equation (5), where the pressure-based sensor is replaced by an analogous term based on the vibrational temperature; additionally, the Ducros sensor is removed to ensure robustness [non ricordo più il motivo, spiegare perché togliamo Ducros]:

$$\varphi_{jV} = \left| \frac{T_{V,j+1} - 2T_{V,j} + T_{V,j-1}}{T_{V,j+1} + 2T_{V,j} + T_{V,j-1}} \right|. \tag{36}$$

For Navier–Stokes simulations, the discretization is completed by a standard fourth-order approximation of the viscous terms. Lastly, time advancement is carried out by means of an explicit third-order TVD Runge–Kutta scheme [19].

4 Results

In this section we validate the thermochemical modeling as well as the numerical strategy by means of selected test cases, ranging from 0D to 2D configurations.

4.1 Zero-dimensional heath baths

The implementation of the 2T model of Park [11] is validated by comparing the results of zero-dimensional (0D) heath baths with reference data. In such a test case, non-equilibrium thermodynamic conditions are initially imposed for the gas mixture; the system then relaxes towards an equilibrium state through dissociation and vibrational relaxation effects. We begin by considering translational-vibrational relaxation with frozen chemistry, in order to assess the behavior of the vibrational source term Q_{TV} uniquely. Figure 1 shows the timewise temperature distributions in a case of vibrational heating (left panel) and vibrational cooling (right panel) for N_2. The initial pressure is equal to $1\,\text{atm}$ for both cases. In the vibrational heating, the initial temperatures are $T^0 = 10000\,\text{K}$ and $T_V^0 = 1000\,\text{K}$ and the system reaches an equilibrium temperature of roughly $7625\,\text{K}$; in the cooling configuration, instead, we set $T^0 = 3000\,\text{K}$ and $T_V^0 = 10000\,\text{K}$, and the equilibrium temperature reached is $\approx 4972\,\text{K}$. The profiles, in excellent agreement with reference results of Casseau $et\ al.$ [20], underline that return to equilibrium is achieved in physical times between 10^{-5} and 10^{-4} seconds. The second set of test cases corresponds to the one investigated by Williams $et\ al.$ [21] and takes into account also dissociation processes. The first heath bath still consists in pure nitrogen with $T^0 = 20000\,\text{K}$, $T_V^0 = 300\,\text{K}$, $p^0 = 27.25\,\text{atm}$ and $Y_{N_2} = 1$ as initial conditions. Figure 2(a) shows the relaxation of the two temperatures up to a physical time of $10^{-6}\,\text{s}$. The results are compared with reference solutions obtained by the softwares SU2-NEMO [22], LeMANS [23] and HTR [24], using different thermochemical formulations and equipped with both preferential and non-preferential dissociation models [25] (only the non-preferential models are shown in figure 2). Both the translational and vibrational temperature profiles are in agreement with the reference solution and relax towards the equilibrium state in approximately the same time. An air mixture is then selected, the initial conditions being $T^0 = 15000\,\text{K}$, $T_V^0 = 300\,\text{K}$, $p^0 = 20.42\,\text{atm}$, $Y_{N_2}^0 = 0.767$ and $Y_{O_2}^0 = 0.233$. The results shown in figure 2(b) exhibit similar discrepancies, with a major scatter on T_V. It is noteworthy to mention that these results are extremely sensitive to the thermochemical models used, as also observed by Williams $et\ al.$. In our formulation, the use of the averaged temperature with $q = 0.7$ may be the principal reason for the discrepancy in time evolution, whereas the final equilibrium state is perfectly predicted. Moreover, Williams $et\ al.$ [21] takes into account the contribution of the electronic energy as well, which is neglected in our work. Nevertheless, when thermochemical models are coupled with the fluid dynamic problem, each model provides a faithful representation, at least for (relatively) low-to-medium temperatures values.
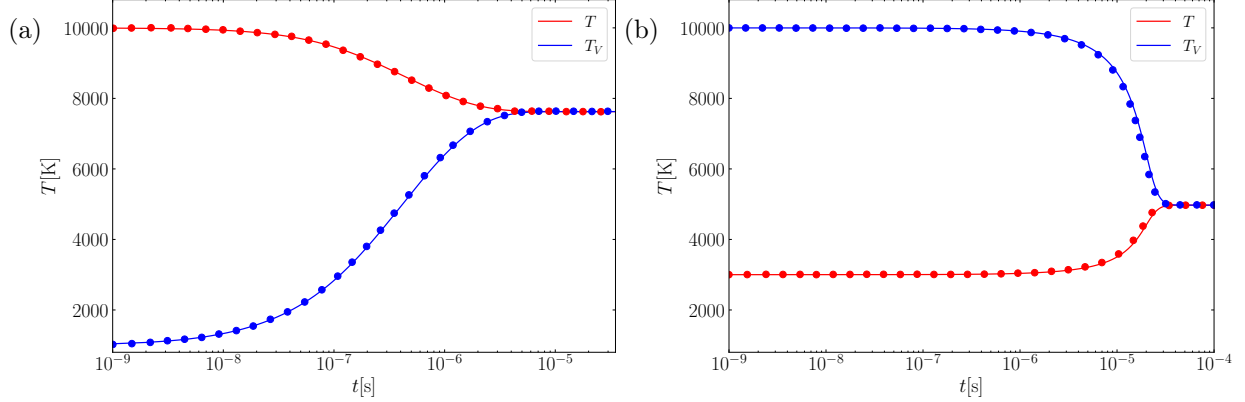
Figure 1: Translational-vibrational relaxation for vibrational heating (a) and vibrational cooling (b) of a N_2 heath bath; symbols from Casseau *et al.* [20].
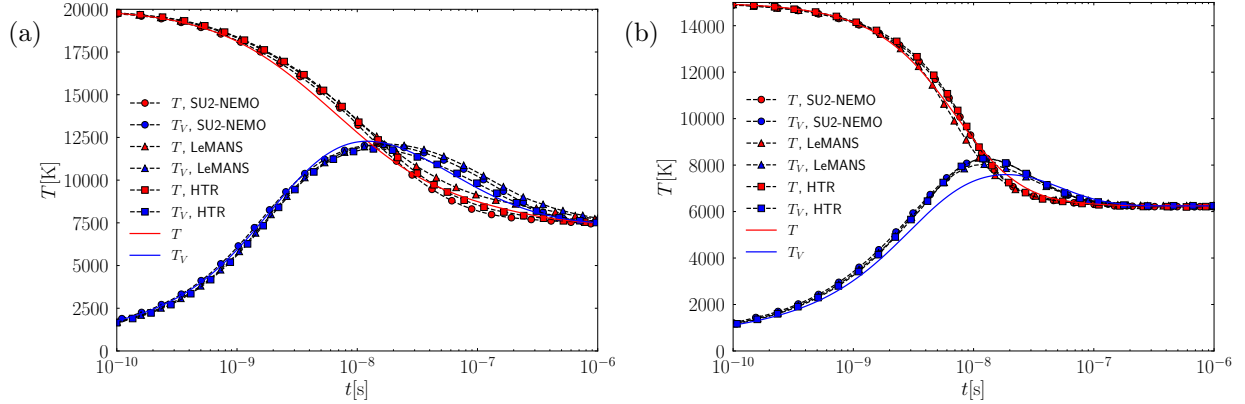

Figure 2: Dissociation/translational-vibrational relaxation heath bath for pure nitrogen (a) and air (b); symbols from Williams *et al.* [21].

4.2 Shock tubes

We now focus our attention on the assessment of the numerical strategy and, in particular, the capability of the shock-capturing method to deal with flow discontinuities. A classical benchmark for such validations is the inviscid one-dimensional shock tube problem. In Sciacovelli *et al.* [2], the numerical strategy was found to correctly reproduce the exact solutions of two perfect-gas shock tube problems and the results of the multi-species high-enthalpy shock tube of Grossman & Cinnella [26]. Even if the latter configuration considers an air mixture under thermochemical non-equilibrium conditions, the flow field was shown not to be affected by thermal nonequilibrium [2], with profiles of pressure, density and velocity essentially unaltered. We have therefore selected a different set of thermodynamic conditions, corresponding to those investigated by Williams *et al.* [21], in which thermal non-equilibrium plays an important role. The left (L) and right (R) initial conditions are the following:

$$P_L = 2\,\text{MPa}, \qquad u_L = 0\,\text{m/s}, \qquad T_L = 12000\,\text{K} \qquad T_{V,L} = 12000\,\text{K} \qquad (37)$$

$$P_R = 100\,\text{kPa}, \qquad u_R = 0\,\text{m/s}, \qquad T_R = 1000\,\text{K} \qquad T_{V,R} = 1000\,\text{K} \qquad (38)$$

whereas the mixture is initially composed of pure molecular nitrogen. The domain has a length of L=1 and it is discretized with 1000 grid points. The system is integrated up to 156 μs of physical time, with a Courant number equal to 0.1. In such a configuration, the shock-capturing approach presented in section 3 with k_2=2 and $k_{2,V}$=0.5 is able to ensure numerical robustness. The evolution of the dimensional values of density,
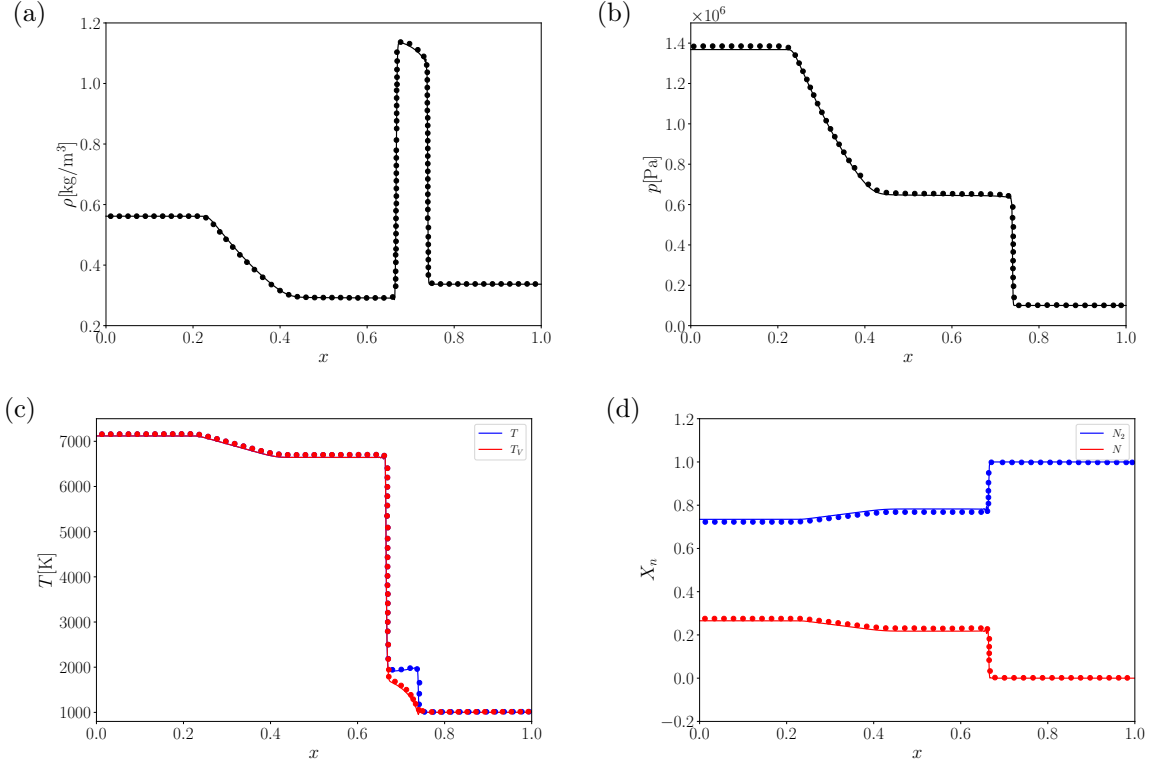
Figure 3: Profiles of density (a), pressure (b), temperatures (c) and molar fractions (d) for the thermochemically out-of-equilibrium shock tube of Williams *et al.* [21], at $156\,\mu$s; symbols from [21].

pressure, temperatures and species molar fractions are displayed in figure 3, where the solution of Williams *et al.* [21] is also reported for reference. The high temperatures in the left side of the tube trigger chemical dissociation; the latter, draining energy from the flow, leads to a decrease of the two temperatures, which equilibrate at $\approx 7000\,$K. A distinct jump of the temperature value is shown at the shock location ($x \approx 0.74$), whereas the vibrational temperature remains frozen and smoothly relaxes after the contact discontinuity. Notwithstanding the presence of small oscillations in the post-shock region, a perfect agreement is observed for all the thermodynamic quantities throughout the computational domain, proving that the numerical strategy is able to handle the computation while correctly capturing shocks and contact discontinuities. For the sake of completeness, we performed another simulation by considering an air mixture with $Y_{N_2} = 0.767$ and $Y_{O_2} = 0.233$, while keeping the other initial conditions unaltered. The results are compared with the pure molecular nitrogen case in figure 4. Significant differences are encountered in all the variables. Dissociation of molecular oxygen is significantly higher, draining internal energy and reducing the temperatures on the left side of the tube below $6000\,$K. Consequently, the pressure is also reduced, whereas the differences in the density profiles are dictated by the different molar fraction composition of the species in the mixture. Thermal nonequilibrium is strongly reduced in the air case, the two temperatures reaching similar values after only $10\,\mu$s; as a result, the density profile exhibits a plateau between the contact discontinuity and the shock. Such a distinct behavior is originated by the different molar fraction composition of the two mixtures and the relaxation times of the diatomic molecules. At the final time, indeed, τ_{N_2} is two orders of magnitude higher than τ_{O_2} and five orders with respect to τ_{NO}, confirming that the presence of the other two molecules promotes a faster recover of thermal equilibrium conditions (as already observed in the work of Passiatore *et al.* [5]).

The last shock tube configuration considered is the two-dimensional viscous case of Daru & Tenaud [27]. An extension of this configuration to a chemically reacting mixture has previously been considered in Sciacovelli *et al.* [2]. The case is then adapted to a thermochemical out-of-equilibrium mixture in the current
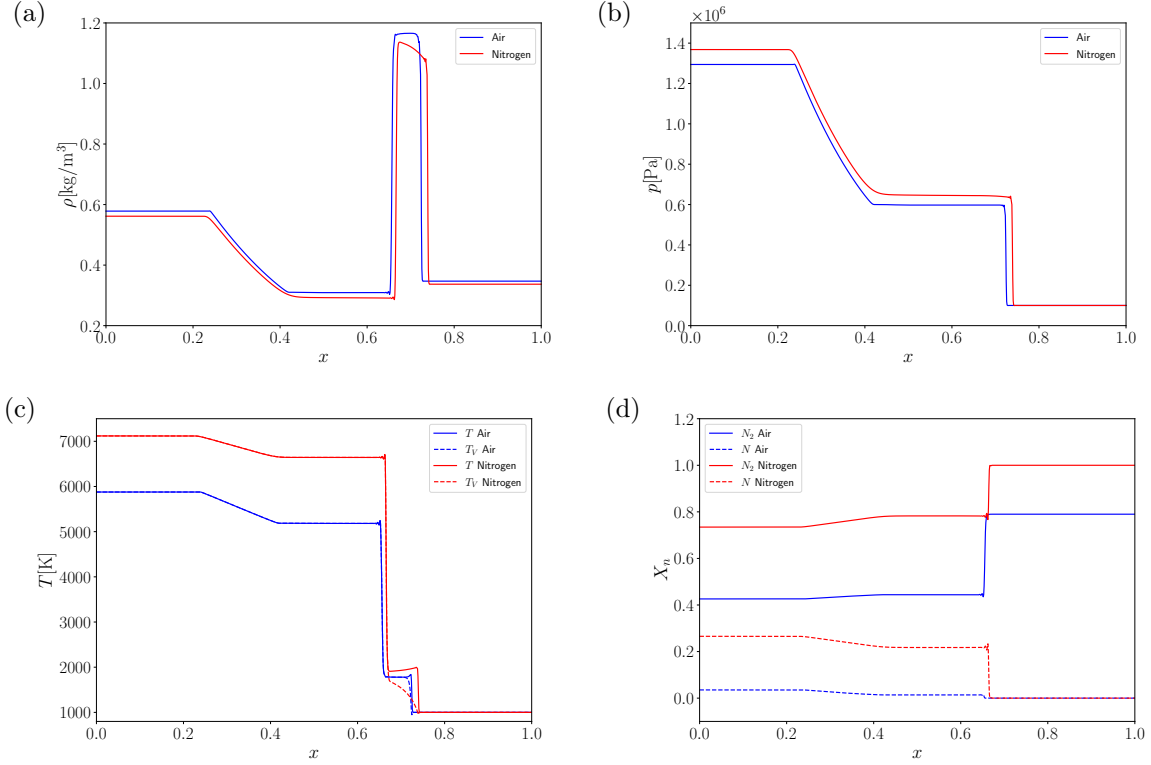
Figure 4: Profiles of density (a), pressure (b), temperatures (c) and molar fractions (d) for the thermochemically out-of-equilibrium shock tube proposed by Williams *et al.* [21], using an air mixture initially composed by $Y_{N_2} = 0.767$ and $Y_{O_2} = 0.233$. Comparison is made against the pure nitrogen simulation.

work. This configuration consists in a rectangular box enclosed within non-catalytic adiabatic walls, with $L_x = 1$ m and $L_y = 0.25$ m as domain lengths. At $t = 0$ s, the flow is divided by a diaphragm at $x = 0.5$ m with the following thermodynamic conditions:

$$P_L = 12 \, \text{kPa}, \qquad u_L = 0 \, \text{m/s}, \qquad T_L = 2000 \, \text{K} \qquad T_{V,L} = 2000 \, \text{K} \tag{39}$$

$$P_R = 0.12 \, \text{kPa}, \qquad u_R = 0 \, \text{m/s}, \qquad T_R = 2000 \, \text{K} \qquad T_{V,R} = 2000 \, \text{K}, \tag{40}$$

and $Y_{N_2} = 0.767$, $Y_{O_2} = 0.233$ everywhere. It is worth noting that we have conserved the same initialization of the chemically-reacting configuration (i.e., air mixture in thermal equilibrium), with $T = T_V = T_{\text{ref}}$, to highlight the influence on the solution when vibrational excitation is taken into account. Uniform computational grids with the same density of those used in Sciacovelli *et al.* [2] are considered (namely, 4000×1000, 6000×1500 and 8000×2000 grid points), with a Courant number set equal to 0.04. In the top panel of figure 5, an instantaneous visualization of the temperatures difference is shown, at $t = 1$ ms. On the left side of the lambda-shock, the flow is vibrationally under-excited and the vibrational temperature is approximately 500 K higher with respect to the translational one. The dynamics of the shock reflected on the right wall generates extremely complex structures that efficiently redistribute the gas and generate an alternation of vibrationally under- and over-excited regions. The bottom panel of figure 5 displays the isocontours of the shock sensor of equation (36) used for the conservative variable ρe_V. The sensor, which is active only on the right part of the shock tube, is able to properly capture T_V gradients, while preserving the fine-scale flow structures and the unsteady dynamics. Globally, the values of φ_{jV} do not exceed 0.2. Figure 6(a) depicts the density profile at the bottom wall of the thermochemical non-equilibrium simulation (TCNE) ad $t = 1$ ms for the three computational grids, showing that a good grid convergence is obtained with 6000×1500. In figure 6(b) instead, a comparison of the wall roto-translational temperature with respect to the thermally equilibrated
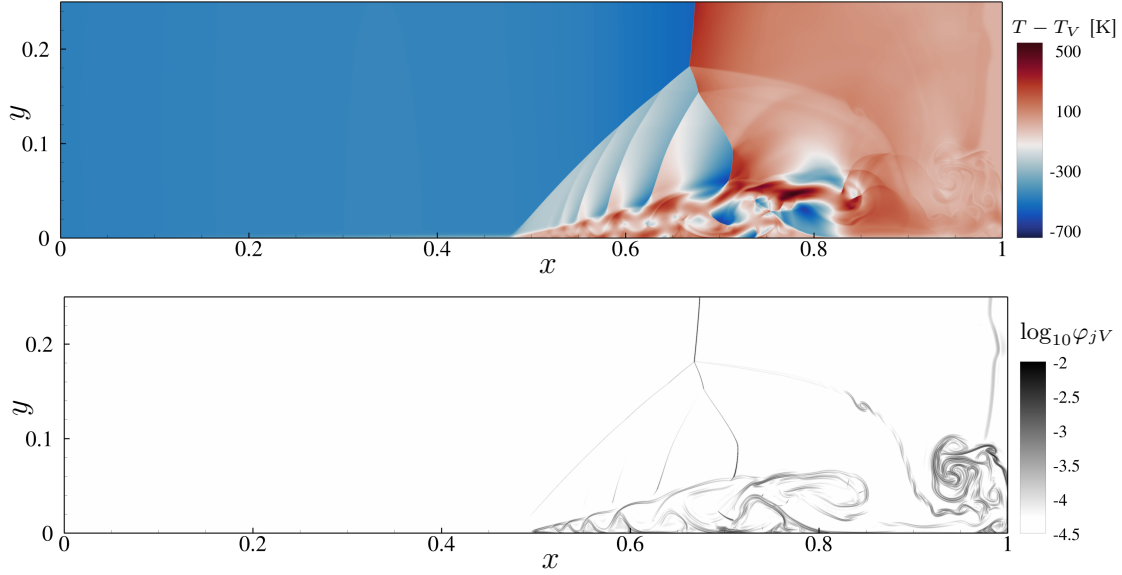
9

Figure 5: Instantaneous visualization of temperatures difference (top) and logarithm of φ_{jV} (bottom), at $t = 1\,\mathrm{ms}$, for the viscous shock tube in thermochemical non-equilibrium.

simulation (CNE) is provided, along with the preferential average $T^{0.7}T_V^{0.3}$ used for the computation of the chemical source terms in the TCNE case. The temperatures difference observed in figure 5(a), due again to the large relaxation times of the N_2 molecule, entails a different distribution with respect to the CNE case especially in the region of Kelvin-Helmotz instabilities. Larger temperature variations are registered for TCNE, with the TCNE preferential averaged temperature sporadically exceeding the CNE temperature (see figure 6(b)) and resulting in peaks of chemical activity and more abundant concentration of chemical products in the TCNE case with respect to the CNE one of Sciacovelli *et al.* [2] (see figure 6(c)-(d)).

4.3   Shock wave boundary layer interaction

The last configuration analyzed consists in a shock wave that impinges on a thermally and chemically out-of-equilibrium, two-dimensional laminar boundary layer. This setup represents a first step towards the simulation of a shock-induced, laminar-to-turbulent flow transition for a three-dimensional domain, motivating the interest for the study of such a configuration. In the following, the deflection angle will be called θ, whereas the shock angle will be denoted with β. The Rankine-Hugoniot conditions will be imposed at the left boundary (inflow) at a specific distance from the leading edge, where appropriate inlet profiles are prescribed. For calorically imperfect gas mixtures, the Rankine-Hugoniot relations have been generalized to an arbitrary equation of state and are iteratively solved to obtain post-shock conditions. Unless otherwise stated, p_w represents the wall pressure normalized with respect to the freestream value, whereas the skin friction coefficient and the Stanton number are expressed by

$$C_f = \frac{\tau_w}{\frac{1}{2}\rho_\infty u_\infty^2} \qquad \text{and} \qquad St = \frac{\lambda \partial T/\partial y}{\rho_\infty u_\infty c_p (T_r - T_w)} \tag{41}$$

where $T_r = T_\infty \left(1 + Pr^{0.5}\frac{\gamma-1}{2}M_\infty^2\right)$. Before assessing the influence of high-enthalpy effects on the shock wave/boundary layer interaction (SWBLI), we aim at testing the numerical strategy by reproducing two different SWBLI configurations available in the literature. First, we consider the configuration analyzed by Sandham *et al.* [28] of a shock-wave interacting with a flat-plate boundary layer at Mach 6. The freestream conditions are $T_\infty = 65\,\mathrm{K}$, $p_\infty = 335.24\,\mathrm{Pa}$, $M_\infty = 6$; the wall temperature is fixed equal to $T_w = 292.5\,\mathrm{K}$. In order to minimize the differences with respect to the reference case, Sutherland's law is used to compute the dynamic viscosity with $T_\mathrm{ref} = 65\,\mathrm{K}$ and $\mu_\mathrm{ref} = 4.335 \times 10^{-6}\,\mathrm{Pa\,s}$, along with a constant Prandtl number
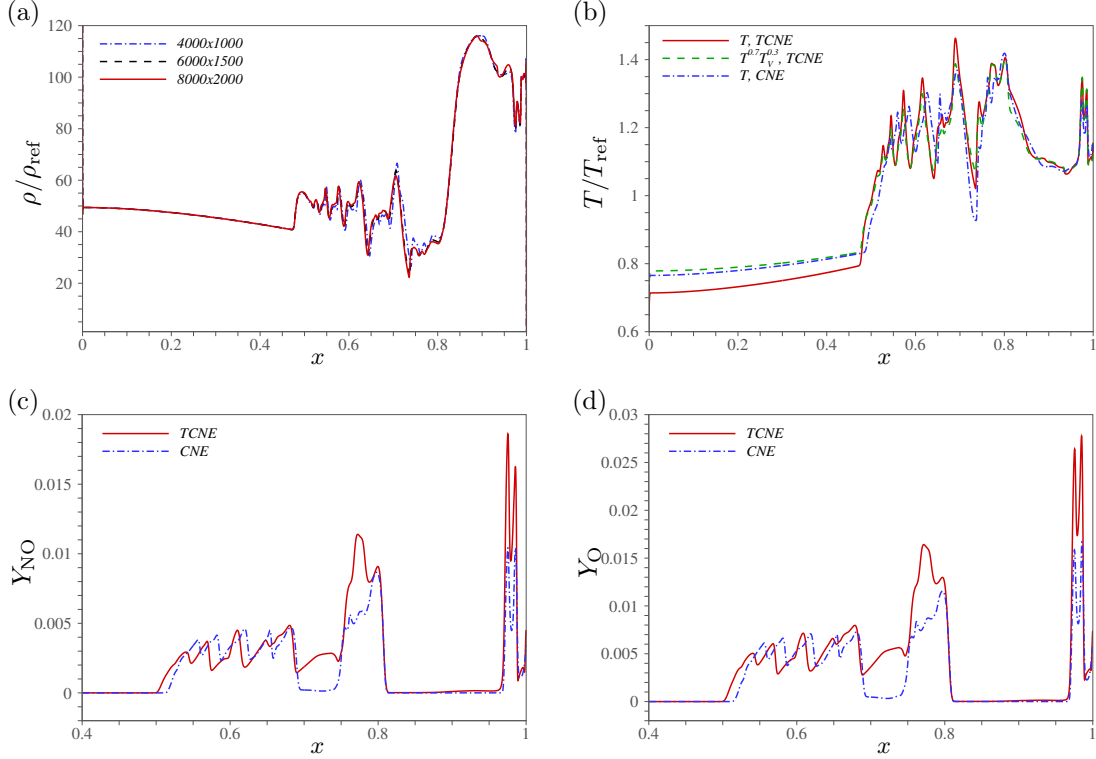
10

Figure 6: Thermochemical non-equilibrium viscous shock tube. Normalized wall density for the three computational grids (a), normalized wall roto-translational temperature (b), nitric oxide mass fraction (c) and atomic oxygen mass fraction (d), compared with the chemically-reacting simulation of [2]. All the profiles are shown at the wall at $t = 1\,\mathrm{ms}$.

equal to 0.72 and a specific heat ratio $\gamma = 1.4$. For the considered freestream conditions, a deflection angle of $\theta = 4°$ generates a shock angle of $\beta \approx 12°$. The shock impinges on the boundary layer at a distance from the leading edge equal to $0.344\,\mathrm{m}$. The profiles of the similarity theory are imposed as inflow boundary condition at a Reynolds number $Re_{x_{\mathrm{in}}} = 31.36 \times 10^4$, corresponding to $Re_{\delta^*_{\mathrm{in}}} = 6830$. The dimensions of the computational domain are $L_x \times L_y = 300\delta^*_{\mathrm{in}} \times 35\delta^*_{\mathrm{in}}$, discretized with 2400 and 300 grid points in the streamwise and wall-normal directions, respectively. A constant grid stretching is applied in the wall-normal direction. Figure 7(a)-(b)-(c) depict the evolutions of the normalized wall pressure, skin friction coefficient and Stanton number, respectively. The results are in excellent agreement with the reference data and faithfully reconstruct the pressure jump, the separation region and the reattachment zone. As a second validation, we consider the SWBLI configuration with finite-rate chemistry simulated by Volpiani [29]. It should be noted that the authors use different thermochemical models and the discrepancies observed in the results are attributed to this. In this case, the freestream thermodynamic conditions are $T_\infty = 2275\,\mathrm{K}$, $p_\infty = 14692\,\mathrm{Pa}$ and $M_\infty = 5.6$; the values of the mass fractions are $Y_{\mathrm{N_2},\infty} = 0.77$ and $Y_{\mathrm{O_2},\infty} = 0.23$ while the wall temperature is set equal to $3042\,\mathrm{K}$. The deflection angle of $6°$ corresponds to a shock angle equal to $\approx 14°$ and the shock impinges on the boundary layer at a distance from the leading edge equal to $0.1\,\mathrm{m}$. The flow is initiated downstream of the leading edge at a distance to $x = 0.001\,\mathrm{m}$, corresponding to $\delta_{99,\mathrm{in}} = 1\,\mathrm{mm}$. At this station, the same inflow profiles of Volpiani [29] are prescribed; that is, a fourth-order polynomial approximation for the velocity and the Crocco-Buseman relation for the temperature with a $\gamma = 1.29$; pressure and species mass fractions are constant and the density is computed from the equation of state. The computational domain is $L_x \times L_y = 200\delta^*_{99,\mathrm{in}} \times 30\delta^*_{99,\mathrm{in}}$, discretized with 2000 and 350 grid points in the streamwise and wall-normal directions, respectively. Note that we use a slightly finer grid with respect to the reference case to avoid any numerical inaccuracy in addition to the thermochemical formulation. Figure 7(d) shows the trend of the normalized wall pressure; despite some discrepancies in the second pressure rise, our
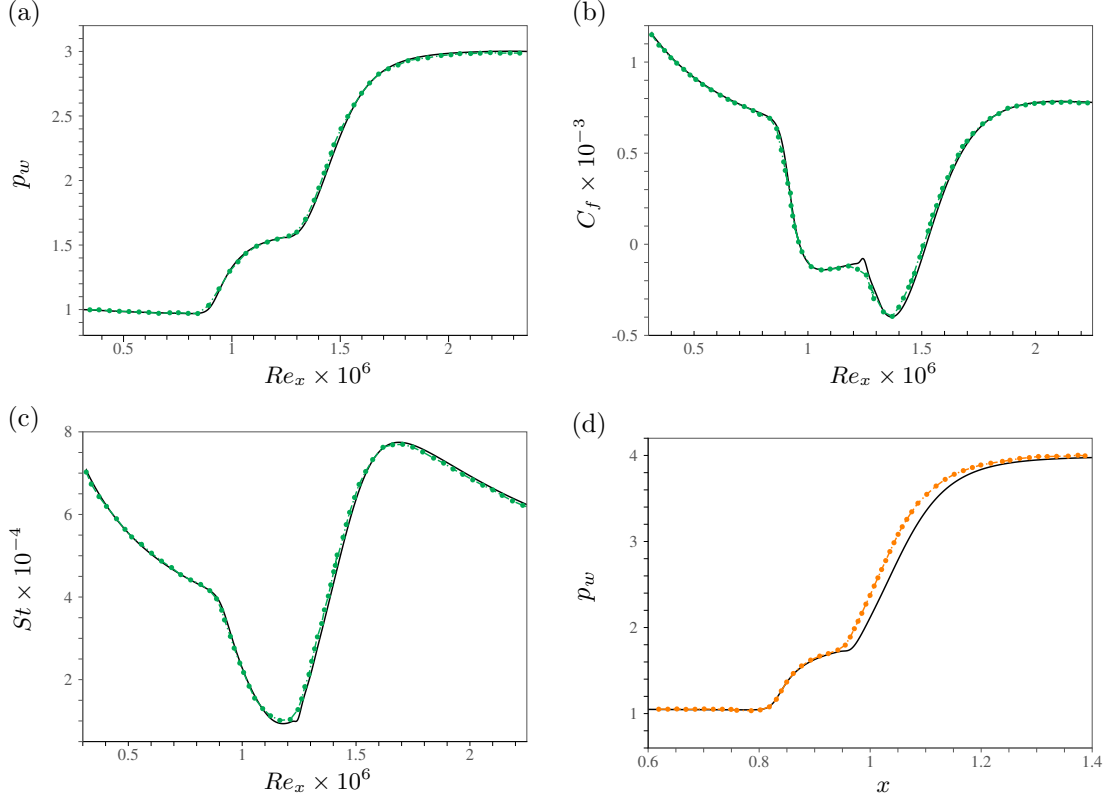
Figure 7: Verification test cases for the SWBLI configuration. Evolution of normalized wall pressure (a), skin friction coefficient (b) and Stanton number (c), compared with the reference solution of Sandham *et al.* [28]. Evolution of normalized wall pressure (d), compared with the reference solution of Volpiani [29].

results are able to match the global pressure jump and are in an acceptable agreement with the reference.

After the validation of the reference results, we focus on the high-enthalpy configuration. The selected setup considers the post-shock condition of a scramjet, approximated by a six degrees planar wedge, flying at Mach 12 at an altitude of 36 km. The corresponding freestream conditions are then $T_\infty = 405\,\mathrm{K}$, $p_\infty = 2258.6\,\mathrm{Pa}$ and $M_\infty = 9$. The wall temperature was fixed equal to $2500\,\mathrm{K}$ for both the translational and vibrational temperature and a non-catalytic condition is imposed for the species mass fractions. The solution of the jump equations with the selected freestream Mach number and $\beta = 10°$, gives $\theta \approx 5°$ and the post-shock (PS) variables $T_{\mathrm{PS}} = 554\,\mathrm{K}$, $p_{\mathrm{PS}} = 6235\,\mathrm{Pa}$ and $u_{\mathrm{PS}} = 3620\,\mathrm{m/s}$. These conditions are imposed at left boundary of the rectangular domain as a jump on the inlet profiles. Specifically, these profiles are obtained by solving the locally self-similar equations reported in Sciacovelli *et al.* [2], extended to thermochemical non-equilibrium. For the sake of reproducibility, we show their trend in figure 8, at a distance of $x_0 = 0.04\,\mathrm{m}$ from the leading edge, corresponding to the beginning of the computational domain for the SWBLI simulation. Figures 8(a)-(b)-(c) displays the evolutions of the two temperatures, velocity and density, normalized with respect to freestream values. A comparison against the solution of the chemically-reacting formulation is also provided and highlights the importance of taking into account vibrational relaxation effects. At these thermodynamic conditions and Reynolds numbers, a significant thermal non-equilibrium is present, with a monotonic profile for the vibrational temperature. The locally self-similar solution is validated against a baseflow simulation (that is, a laminar boundary layer without shock impingement) by comparing the resulting skin friction coefficient in figure 8(d). The extent of the computational domain is $L_x \times L_y = 1200\delta_{\mathrm{in}}^* \times 90\delta_{\mathrm{in}}^*$, with $\delta_{\mathrm{in}}^* = 1.77 \times 10^{-3}\,\mathrm{m}$. As for the discretization, three computational grids have been considered, namely $N_x \times N_y = 3000 \times 256$ for the coarse grid, $N_x \times N_y = 5120 \times 360$ for the medium grid and $N_x \times N_y = 8280 \times 512$ for the finest one. A constant grid stretching is applied in the wall-normal direction, with the first wall cell being equal to $3.5 \times 10^{-5}\,\mathrm{m}$, $3 \times 10^{-5}\,\mathrm{m}$ and $2 \times 10^{-5}\,\mathrm{m}$ for the three computational
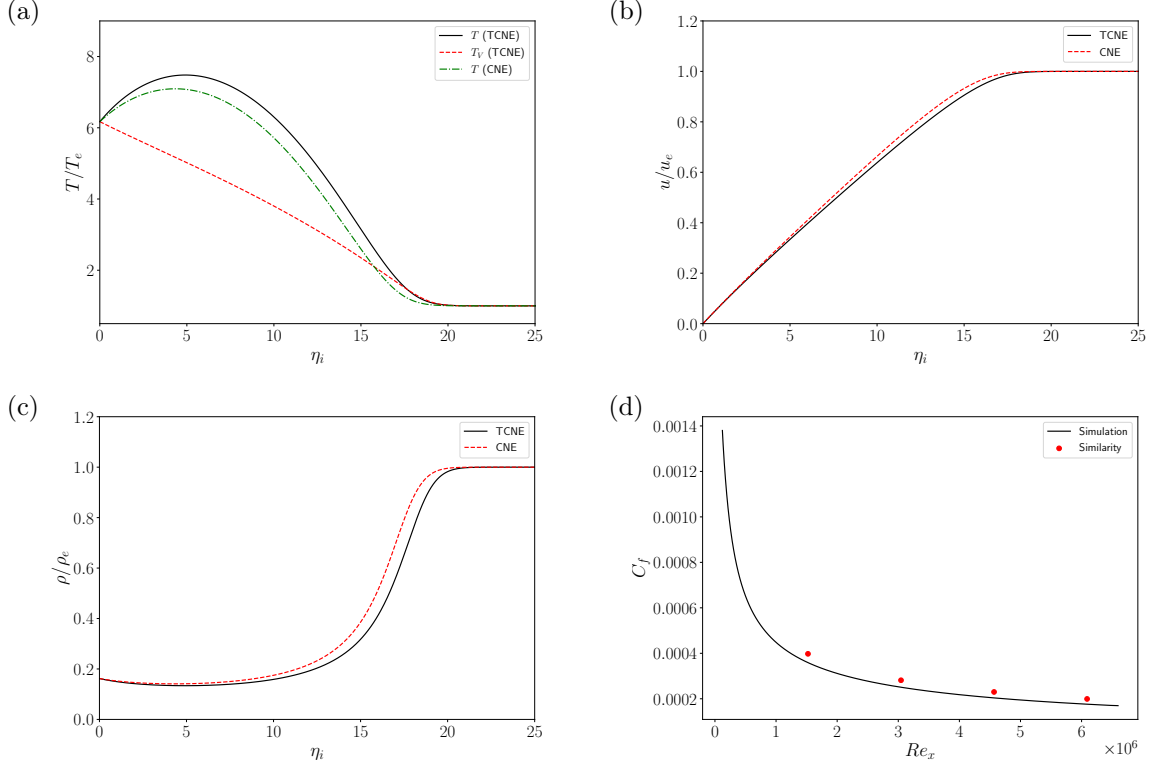
Figure 8: Evolution of normalized temperatures (a), normalized velocity (b), normalized density (c), computed from the locally self-similar theory at $x = 0.04$ m. Comparison between simulation results and locally-self similar theory of the skin friction coefficient (d).
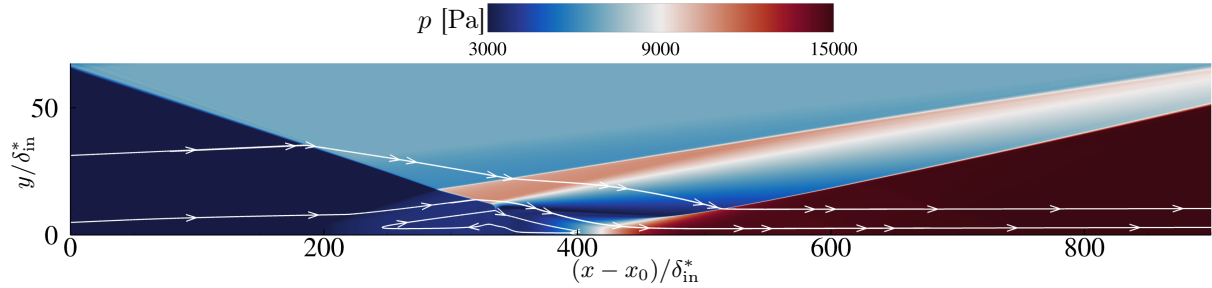

Figure 9: Instantaneous visualization of the pressure field for the proposed SWBLI simulation in thermochemical non-equilibrium. In the figure, we display three streamlines which mark the separation bubble, the flow surrounding the recirculation zone and the dynamics of the far field, respectively.

grids, respectively. The impingement station is set equal to 0.7 m. The pressure isocontour shown in figure 9 gives an idea of the configuration under analysis. The incident shock creates a recirculation bubble (marked in the figure) in which the flow separates. Upstream of the separation bubble, a series of compression waves occur, which then coalesce into the separation shock. The latter interacts with the incident shock that penetrates the separated flow and is reflected as an expansion fan. Downstream of the separation bubble, a new shock (usually referred-to as reattachment shock) occurs, which readjusts the previously deflected flow. For a better understanding of the dynamics, three streamlines are also marked, one surrounding the recirculation bubble and the other two at larger wall-normal locations.

The evolutions of the skin friction coefficient and of the normalized wall pressure are reported in figure 10.
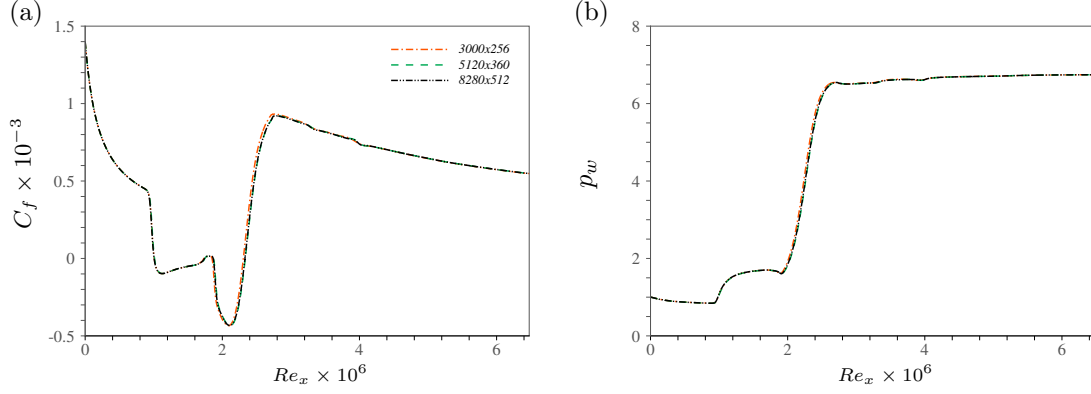
Figure 10: Evolution of the skin friction coefficient (a) and normalized wall pressure (b) for the proposed SWBLI in thermochemical non-equilibrium.
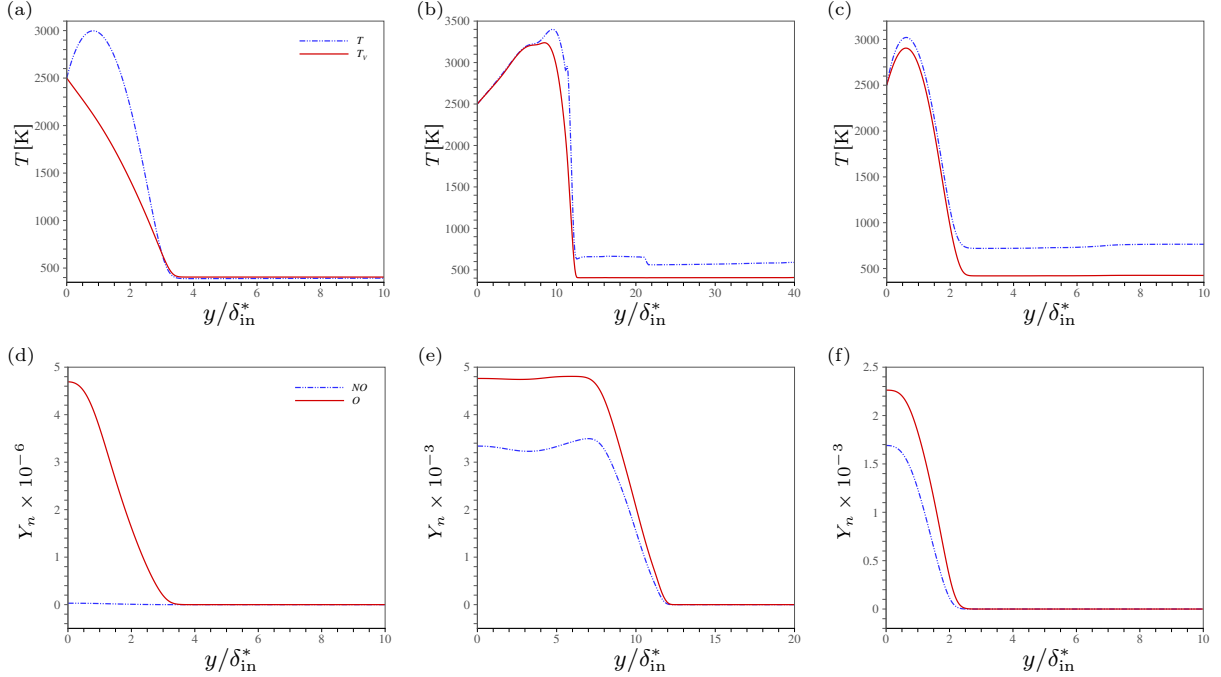

Figure 11: Wall-normal evolution of temperatures (a-b-c) and major products in the mixture (d-e-f) for three stations extracted before the impingement at $Re_x \approx 6.3 \times 10^5$ (a-d), in the separation bubble at $Re_x \approx 1.8 \times 10^6$ (b-e) and after the reflected shock $Re_x \approx 4 \times 10^6$ (c-f).

The comparison between the three computational grids shows that grid-converged results are obtained already with the medium refinement. By analyzing the evolution of the wall quantities, it is possible to note that the interaction begins at $Re_x \approx 8 \times 10^5$, where the wall pressure distribution suddenly rises while C_f decreases. Thereafter, the separation bubble extends from this point up to $Re_x \approx 2 \times 10^6$. The subsequent increase of C_f and p_w indicates the reattachment zone, before relaxing towards the new undisturbed conditions. The characteristic features of SWBLI configuration are not altered by high-enthalpy effects and the present numerical method is shown to be able to handle the strong pressure gradients using $k_2 = 1.5$ and $k_{2,V} = 0.5$. More interesting is instead the effect of this complex dynamics on thermal and chemical activities. Figure 11 depicts the evolution of the two temperatures and of the major products in the mixture before the impingement at $Re_x \approx 6.3 \times 10^5$, in the separation bubble at $Re_x \approx 1.8 \times 10^6$ and after the reflected shock at
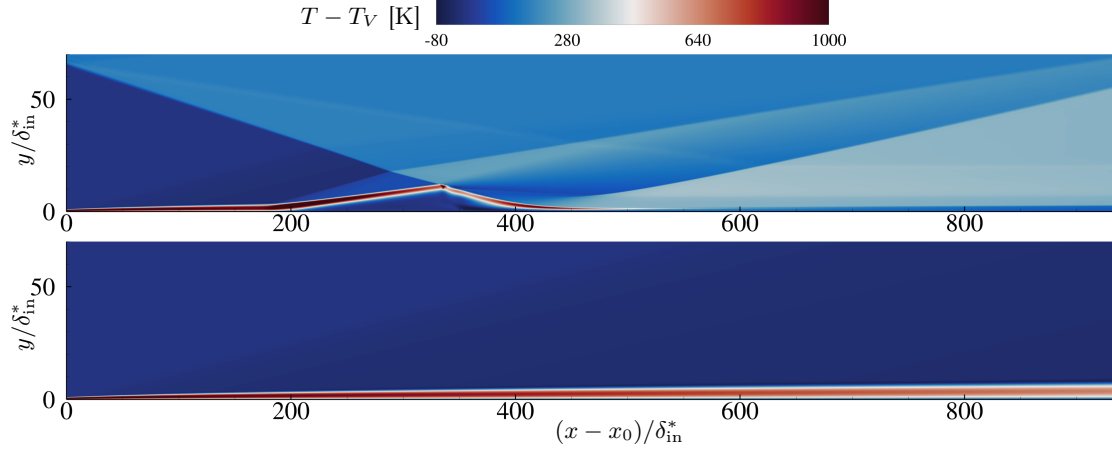
Figure 12: Instantaneous visualization of temperatures difference for the SWBLI in thermochemical non-equilibrium (top) and the corresponding simulation without shock impingement (bottom).

$Re_x \approx 4 \times 10^6$. Coherently with the inlet temperature profiles, the amount of thermal non-equilibrium before the bubble is extremely high while chemical activity is essentially negligible. The rise of the temperatures and pressure in the separation zone promotes a more significant chemical dissociation but, at the same time, the gap between the two temperatures becomes smaller, moving towards a situation of quasi thermal equilibrium right after the recirculation bubble. Of note, the two temperatures keep distinct values at the edge of the boundary layer and in the undisturbed flow. A comparison with the same boundary layer without shock impingement has revealed that, for such thermodynamic conditions and Reynolds numbers, the flow would remain in a state of thermal non-equilibrium and quasi frozen chemical activity inside the entire boundary layer. The effect of pressure rise has then reduced the amount of thermal non-equilibrium and promoted the chemical activity with respect to the case without incident shock. Figure 12 shows the isocontours of the temperatures difference for the current configuration (top) and for the corresponding base flow, in order to better appreciate the different thermochemical features promoted by the shock wave impingement.

5   Conclusions

In this study, a simple and robust numerical strategy for carrying out high-fidelity simulations of high-enthalpy flows has been presented and validated. The present approach builds upon the numerical scheme described in Sciacovelli *et al.* [2], initially proposed for chemical nonequilibrium configurations, and extends it to take into account vibrational relaxation processes. For such configurations, the original shock sensor, based on a combination of Ducros' and Jameson's pressure-based sensors, is unsuitable to control the shock-capturing term in the vibrational energy equation because of the loose coupling between vibrational temperature and pressure. As a consequence, a modified sensor based on the vibrational temperature is proposed, and its performances are assessed against a selected test cases of increasing complexity.

The thermochemical models implemented in the in-house CFD solver are first validated by means of several zero-dimensional heat baths. The vibrational heating and cooling of a N_2 molecule with frozen chemistry is validated against the data of Casseau *et al.* [20]; then, the coupled vibrational and finite-rate chemistry models are tested in the heat baths of pure nitrogen and air described by Williams *et al.* [21]. The results, highly sensitive to the particular model used, show a fair agreement with the reference ones. Afterwards, a 1D shock tube configuration exhibiting thermal nonequilibrium is investigated. The profiles of density, pressure, temperatures and mass fractions at the final time are in excellent agreement with those obtained by Williams *et al.* [21], confirming the capabilities of the numerical scheme to correctly handle strong shocks and contact discontinuities. The simulation is repeated by using an air-mixture instead of pure molecular nitrogen, showing that thermal nonequilibrium is drastically reduced because of the rapid dissociation of O_2 and the much faster relaxation times of O_2 and NO with respect to N_2. The last shock tube setup considered

concerns the thermochemical extension of the 2D viscous case described in Sciacovelli et al. [2]. The comparison between thermal nonequilibrium and thermally equilibrated conditions highlights the importance of taking into account vibrational relaxation processes, the difference between the two temperatures reaching values larger than 500 K.

The last test case considered deals with a 2D shock-wave/boundary layer interaction (SWBLI). The numerical setup is first validated against the results of Sandham *et al.* [28], for the low-enthalpy configuration, and of Volpiani [29], taking into account finite-rate chemistry effects. Then, we focus on a high-enthalpy case representing the post-shock conditions of a scramjet flying at Mach 12 at an altitude of 36 km, with a wall temperature of 2500 K. The locally self-similar profiles imposed at the inflow reveal strong thermal non-equilibrium and a mild chemical activity. The increase in temperature and pressure in the separation region tends to reverse the inlet trends, albeit a difference in the two temperatures persists at the edge of the boundary layer. A comparison with an unperturbed 2D boundary layer confirms that the presence of the incident shock leads to a reduced thermal non-equilibrium and promote chemical processes. Future work will address a 3D SWBLI configuration undergoing laminar-to-turbulent transition, with focus on interactions between thermochemical effects and turbulence in a shocked configuration, and the application of the present methodology to more complex multi-temperature models.

References

[1] G. Candler. Rate effects in hypersonic flows. *Annual review of Fluid Mechanics*, 51:379–402, 2019.

[2] L. Sciacovelli, D. Passiatore, P. Cinnella, and G. Pascazio. Assessment of a high-order shock-capturing central-difference scheme for hypersonic turbulent flow simulations. *Computers & Fluids*, 230(105134):1–23, 2021.

[3] A. Jameson, W. Schmidt, and E. Turkel. Numerical solutions of the Euler equations by finite volume methods using Runge-Kutta time-stepping schemes. *AIAA Journal*, 81(1259), 1981.

[4] L. Sciacovelli, X. Gloerfelt, D. Passiatore, P. Cinnella, and F. Grasso. Numerical investigation of high-speed turbulent boundary layers of dense gases. *Flow, Turbulence and Combustion*, 105(2):555–579, 2020.

[5] Donatella Passiatore, Luca Sciacovelli, Paola Cinnella, and G Pascazio. Thermochemical non-equilibrium effects in turbulent hypersonic boundary layers. *Journal of Fluid Mechanics*, 941, 2022.

[6] P. A. Gnoffo, R. N. Gupta, and J. L. Shinn. Conservation equations and physical models for hypersonic air flows in thermal and chemical nonequilibrium. 1989.

[7] C. Park. Two-temperature interpretation of dissociation rate data for N2 and O2. In *26th Aerspace Sciences Meeting*, page 458, 1988.

[8] C. Park. *Nonequilibrium Hypersonic Aerothermodynamics*. John Wiley and Sons, 1990.

[9] R. C. Millikan and D. R. White. Systematics of vibrational relaxation. *Journal of chemical physics*, 39:3209–3213, 1963.

[10] C. Park. Review of chemical-kinetic problems of future NASA missions. I-Earth entries. *Journal of Thermophysics and Heat transfer*, 7(3):385–398, 1993.

[11] C. Park. Assessment of two-temperature kinetic model for ionizing air. *Journal of Thermophysics and Heat Transfer*, 3(3):233–244, 1989.

[12] F. G. Blottner, M. Johnson, and M. Ellis. Chemically reacting viscous flow program for multi-component gas mixtures. Technical report, Sandia Laboratory, 1971.

[13] J. O. Hirschfelder and C. F. Curtiss. *Molecular theory of gases and liquids*. John Wiley and Sons, 1969.

[14] C. R. Wilke. A viscosity equation for gas mixtures. *The journal of chemical physics*, 18(4):517–519, 1950.

[15] T. Poinsot and D. Veynante. *Theoretical and numerical combustion*. RT Edwards, Inc., 2005.

[16] R. N. Gupta, J. M. Yos, R. A. Thompson, and KP Lee. A review of reaction rates and thermodynamic and transport properties for an 11-species air model for chemical and thermal nonequilibrium calculations to 30000 K. 1990.

[17] F. Ducros, V. Ferrand, F. Nicoud, C. Weber, D. Darracq, C. Gacherieu, and T. Poinsot. Large-eddy simulation of the shock/turbulence interaction. *Journal of Computational Physics*, 152(2):517–549, 1999.

[18] A. Bhagatwala and S.K. Lele. A modified artificial viscosity approach for compressible turbulence simulations. *Journal of Computational Physics*, 228(14):4965–4969, 2009.

[19] S. Gottlieb and C.-W. Shu. Total variation diminishing runge-kutta schemes. *Mathematics of computation*, 67(221):73–85, 1998.

[20] V. Casseau, D. ER Espinoza, T. J. Scanlon, and R. E. Brown. A two-temperature open-source cfd model for hypersonic reacting flows, part two: multi-dimensional analysis. *Aerospace*, 3(4):45, 2016.

[21] C Williams, M Di Renzo, and J Urzay. Two-temperature extension of the htr solver for hypersonic turbulent flows in thermochemical nonequilibrium.

[22] Walter T Maier, Jacob T Needels, Catarina Garbacz, Fábio Morgado, Juan J Alonso, and Marco Fossati. Su2-nemo: an open-source framework for high-mach nonequilibrium multi-species flows. *Aerospace*, 8(7):193, 2021.

[23] L. C. Scalabrin. *Numerical simulation of weakly ionized hypersonic flow over reentry capsules*. PhD thesis, Citeseer, 2007.

[24] M. Di Renzo, L. Fu, and J. Urzay. HTR solver: An open-source exascale-oriented task-based multi-GPU high-order code for hypersonic aerothermodynamics. *Computer Physics Communications*, 255:107262, 2020.

[25] S. P. Sharma, W. M. Huo, and C. Park. Rate parameters for coupled vibration-dissociation in a generalized ssh approximation. *Journal of thermophysics and heat transfer*, 6(1):9–21, 1992.

[26] B. Grossman and P. Cinnella. Flux-split algorithms for flows with non-equilibrium chemistry and vibrational relaxation. *Journal of Computational Physics*, 88(1):131–168, 1990.

[27] V. Daru and C. Tenaud. Numerical simulation of the viscous shock tube problem by using a high resolution monotonicity-preserving scheme. *Computers & Fluids*, 38(3):664–676, 2009.

[28] ND Sandham, Erich Schülein, Andrew Wagner, Sebastian Willems, and Johan Steelant. Transitional shock-wave/boundary-layer interactions in hypersonic flow. *Journal of Fluid Mechanics*, 752:349–382, 2014.

[29] PS Volpiani. Numerical strategy to perform direct numerical simulations of hypersonic shock/boundary-layer interaction in chemical nonequilibrium. *Shock Waves*, 31(4):361–378, 2021.